

Modelling tephra dispersal and ash aggregation: The 26th April 1979 eruption, La Soufrière St. Vincent

M. Poret^{a,b,*}, A. Costa^a, A. Folch^c, A. Martí^c

^a Istituto Nazionale di Geofisica e Vulcanologia, Sezione di Bologna, Bologna, Italy

^b University of Bologna, Geophysics Department, Bologna, Italy

^c CASE Department, Barcelona Supercomputing Center, Barcelona, Spain

ARTICLE INFO

Article history:

Received 8 May 2017

Received in revised form 12 September 2017

Accepted 17 September 2017

Available online 22 September 2017

Keywords:

Tephra fallout

Volcanic ash

Aggregation

TGSD

FALL3D

WRF/ARW

Eruption Source Parameters

La Soufrière St. Vincent

ABSTRACT

On the 26th April 1979, La Soufrière St. Vincent volcano (West Indies) erupted producing a tephra fallout that blanketed the main island and the neighboring Bequia Island, located southwards. Using deposit measurements and the available observations reported in Brazier et al. (1982), we estimated the optimal Eruption Source Parameters, such as the Mass Eruption Rate (MER), the Total Erupted Mass (TEM) and the Total Grain-Size Distribution (TGSD) by means of a computational inversion method. Tephra transport and deposition were simulated using the 3D Eulerian model FALL3D. The field-based TGSD reconstructed by Brazier et al. (1982) shows a bi-modal pattern having a coarse and a fine population with modes around 0.5 and 0.06 mm, respectively. A significant amount of aggregates was observed during the eruption. To quantify the relevance of aggregation processes on the bulk tephra deposit, we performed a comparative study in which we accounted for aggregation using three different schemes, computing ash aggregation within the plume under wet conditions, i.e. considering both the effects of air moisture and magmatic water, consistently with the eruptive phreatomagmatic eruption features. The sensitivity to the driving meteorological model (WRF/ARW) was also investigated by considering two different spatial resolutions (5 and 1 km) and model output frequencies. Results show that, for such short-lived explosive eruptions, high-resolution meteorological data are critical. Optimal results best-fitting all available observations indicate a column height of ~12 km above the vent, a MER of $\sim 7.8 \times 10^6$ kg/s which, for an eruption duration of 370 s, gives a TEM of $\sim 2.8 \times 10^9$ kg. The optimal aggregate mean diameter obtained is 1.5ϕ with a density of 350 kg/m³, contributing to ~22% of the deposit mass.

© 2017 Elsevier B.V. All rights reserved.

1. Introduction

Volcanic plumes generated from explosive eruptions can rise up to tens of kilometers above the vent (hereinafter a.v.) injecting large amounts of tephra into the atmosphere. The erupted particulate material has diameters (d) varying by several orders of magnitude. Tephra is classified according to fragment diameter differentiating blocks ($d > 64$ mm) from lapilli ($2 \text{ mm} < d < 64 \text{ mm}$) and ash ($d < 2 \text{ mm}$). Ash is further classified as coarse ash for particles with $64 \mu\text{m} < d < 2 \text{ mm}$, fine ash for $d < 64 \mu\text{m}$, and very fine ash for $d < 31 \mu\text{m}$ (Rose and Durant, 2009). The particle Grain-Size Distribution (GSD) together with the atmospheric conditions control the sedimentation processes and, consequently, the tephra residence time in the atmosphere. However, particle-particle interactions leading to aggregation can occur thereby affecting the transport dynamics. In addition, aggregation

processes can potentially increase the hazards induced by tephra fallout on infrastructures and inhabitants in the vicinity of a volcano. Tephra dispersal models neglecting aggregation phenomena may result on a significant ground loading underestimation at proximal areas and overestimation at distal locations (Brown et al., 2012; Van Eaton et al., 2012; Folch et al., 2016).

On 26th April 1979, La Soufrière St. Vincent volcano (West Indies) produced a phreatomagmatic eruption due to interaction between the shallow aquifer and magma. The phreatomagmatic phase of the eruption produced a significant amount of aggregates, which were observed in-situ during fallout and were also evident from the grain-size features of the collected samples. Indeed, tephra deposits showed a rich fine ash composition at proximal and medial locations (Brazier et al., 1982, 1983). Despite these observations, quantifying aggregation formed within a volcanic plume from field data is a challenging task due to the aggregates tendency to disaggregate when impacting the ground (Brazier et al., 1982). At the end of the eruption, 33 field samples were collected providing tephra loadings at each location (Fig. 1a). These samples are valuable to constrain simulations and quantify the role of ash aggregation combining field measurements and models.

* Corresponding author at: Istituto Nazionale di Geofisica e Vulcanologia, Sezione di Bologna, Bologna, Italy.

E-mail address: matthieu.poret@gmail.com (M. Poret).

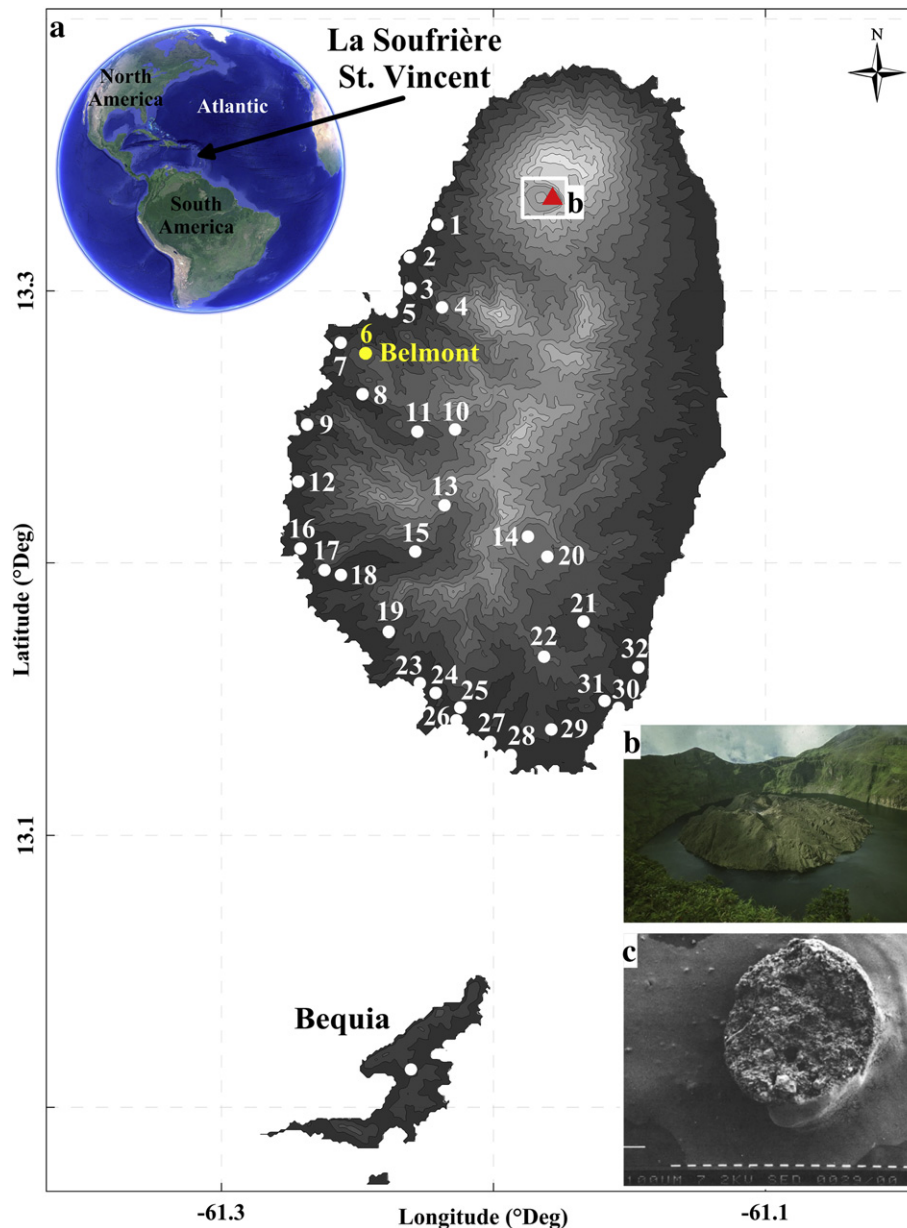


Fig. 1. a) Location of La Soufrière St. Vincent volcano (West Indies). White dots are sample locations (detailed in Table 1) from the vent (red triangle) to Bequia Island. Location n°6 refers to the Belmont observatory (yellow dot). b) Photo of the permanent lake inside the summit crater before the April 1979 eruptive activity. Source: André Guyard. c) Example accretionary lapillus observed during the eruption. White bars are 100 μm in length. (Modified from Brazier et al., 1982)

Eruption Source Parameters (ESP) such as the eruption column height, the Total Grain-Size Distribution (TGSD), the eruption start time and duration are needed as inputs by tephra dispersal and deposition models. This study uses FALL3D (Costa et al., 2006; Folch et al., 2009, 2012), a 3D time-dependent Eulerian model based on the numerical solution of the advection-diffusion-sedimentation equation to best-fit the ESPs using the available measurements. Simulations are initialized using, for each ESP, a range of values derived from Brazier et al. (1982) and a high resolution meteorological model (at 1 km horizontal resolution) as driver of the FALL3D model. The TGSD description is highly dependent on the sampling distance from the vent (Costa et al., 2016a) but also on the spatial distribution of samples and the density of outcrops (Bonadonna et al., 2015; Spanu et al., 2016).

This paper investigates the relevance of aggregation processes on the bulk tephra deposit for the 26th April 1979 La Soufrière St. Vincent eruption. Different TGSDs are evaluated, including: i) the field-based TGSD

derived from the sample analysis; ii) a parameterization of the latter using a bi-lognormal distribution and; iii) using a bi-Weibull distribution (Costa et al., 2016a, 2017). Simulations also account for aggregation by considering three different aggregation schemes implemented in FALL3D. Results are compared with simulations in which aggregation is neglected. ESP optimal values are obtained through a computational inversion method previously presented by Folch et al. (2010) and Martí et al. (2016). Simulation results are compared with field measurements by employing a criterion as the goodness-of-fit measure test, which selects consistent results that better reproduce the measured tephra loadings.

Section 2 provides a short overview of the eruption. In Section 3, we describe the computational model and methodology. Section 4 presents the results of the comparative study on different TGSDs and aggregation schemes. Finally, Section 5 discusses the results in terms of effect of the parameterization used to reconstruct the main features of a short-lived explosive eruption.

2. April 26th 1979 eruption - La Soufrière St. Vincent

The 1979 La Soufrière St. Vincent eruptions started on the 8th April and lasted for more than two weeks with 11 eruption columns (Shepherd and Sigurdsson, 1982; Brazier et al., 1982, 1983). Since the previous event on 1971, a lava dome had slowly grown in the middle of the ~1.6 km wide summit crater lake (Fig. 1b), creating an island that gradually filled up the crater. On the 26th April, a short-lived violent eruption started at 03:58 UTC (midnight LT) and lasted up to 04:04 UTC, with a duration of 370 s (~6 min) according to the seismic records of the volcanic tremor signal. Meteorological observations reported a cloudless night with no rain. Brazier et al. (1982) estimated the first eruptive column height around 7–8 km above sea level (hereinafter a.s.l.) during the first minutes, which was measured from the Belmont Observatory (~10 km far from the vent, label 6 on Fig. 1a). Then, the plume rose up to ~14 km a.s.l., giving an approximate rise velocity of around 25–30 m/s. The plume was strongly controlled by northerly winds that dispersed tephra southwards blanketing most of St. Vincent and Bequia Islands. The short duration of the 26th April event allowed the observation of a rapid disconnection of the rising plume from the vent of ~2–3 km after a few minutes (Brazier et al., 1982, Fig. 14 therein). Then, satellite observations showed a split of the plume into a major and a minor lobe. The latter one spread eastwards over the sea with no possibility for the tephra fallout to be sampled. In contrast, soon after the eruption the major lobe was sampled at 32 locations on the main island and 1 on Bequia Island (Fig. 1a and Table 1). Deposit samples were analyzed using the sieving method (Walker, 1971) down to $d = 90 \mu\text{m}$ with a 0.5Φ interval (where $\Phi = -\log_2 d$, with d in mm) and, for ash finer than $90 \mu\text{m}$, employing the electrosensing zone method with an Elzone celloscope as described by Muerdter et al. (1981).

One remarkable feature of this eruption was the formation of a significant amount of loose and weakly bounded aggregates and accretionary lapillus (Fig. 1c). Due to disintegration processes during tephra fallout, in-situ observations (Brazier et al., 1982) estimated only an aggregate fraction of 10% (accretionary lapillus), with a mean diameter between 1 and 3 mm. Brazier et al. (1982) showed that most of the collected samples clearly had a bi-modal distribution and reported the GSD of 4 samples (labels 3, 6, 25 and Bequia in Fig. 1a), which show a fine sub-population mode at $4-5\Phi$. These samples are used for a comparative study against the computed GSDs at the sample locations.

3. Computational models and best-fitting methodology

3.1. Tephra dispersal and plume models

Tephra deposits for the 26th April 1979 St. Vincent eruption are reconstructed using the tephra dispersal model FALL3D. The model requires the eruption source term parameters of the event together with the meteorological data over the corresponding domain (Fig. 1a). We use the integral plume model available in FALL3D (FPlume; Folch et al., 2016) to obtain the MER and the effective particle Grain-Size Distribution resulting from wet aggregation occurring within the plume. FPlume is based on the Buoyant Plume Theory (Morton et al., 1956) accounting for wind coupling, air moisture effects and particle re-entrainment, which may strongly affect tephra particle distribution along the plume. As input, the plume model requires information about the magma water content and the initial magma temperature. However, FPlume does not account for disaggregation phenomena, i.e. decomposing aggregates from particle collisions, implying that aggregates are transported and deposited without being altered (Folch et al., 2016). In our context, La Soufrière St. Vincent is a basaltic-andesitic

Table 1

Coordinates of the 33 samples with the corresponding tephra loadings. The computed loadings are related to the optimal results for the three input TGSDs (Brazier, bi-Gaussian and bi-Weibull TGSDs, respectively) under the Costa aggregation scheme (bottom panels in Fig. 6).

Field observations				Computed loadings (kg/m ²)		
Location	X (°Deg)	Y (°Deg)	Load (kg/m ²)	Brazier TGSD	bi-Gaussian	bi-Weibull
1	−61.221877	13.321861	8.94	–	–	–
2	−61.231127	13.313686	14.15	–	–	–
3	−61.230555	13.301077	4.82	0.85	0.77	0.85
4	−61.218897	13.294033	5.25	3.94	3.40	3.80
5	−61.23738	13.292358	5.22	0.47	0.45	0.51
6	−61.247055	13.277122	0.95	0.60	0.61	0.69
7	−61.256228	13.28102	0.56	0.33	0.33	0.37
8	−61.248063	13.262062	1.06	0.57	0.61	0.68
9	−61.268513	13.250857	0.43	0.35	0.37	0.40
10	−61.214102	13.249161	1.79	6.69	6.71	7.61
11	−61.228019	13.248297	1.45	2.50	2.60	2.91
12	−61.27176	13.230013	0.30	0.14	0.15	0.15
13	−61.218021	13.221249	2.32	3.47	3.56	3.90
14	−61.18733	13.209672	1.91	2.79	2.90	3.28
15	−61.228753	13.204211	0.73	1.76	1.75	1.75
16	−61.270987	13.205405	0.23	0.67	0.65	0.62
17	−61.262154	13.197381	0.51	0.66	0.64	0.59
18	−61.256024	13.195622	0.44	0.71	0.68	0.63
19	−61.238466	13.174846	0.66	1.70	1.60	1.45
20	−61.180231	13.202388	1.73	2.02	2.10	2.37
21	−61.166841	13.178468	1.13	0.76	0.78	0.86
22	−61.181437	13.165772	1.10	1.03	1.02	1.00
23	−61.227063	13.155969	1.02	1.86	1.75	1.53
24	−61.221264	13.152389	0.95	1.85	1.74	1.51
25	−61.212177	13.147087	0.89	1.50	1.40	1.21
26	−61.21363	13.142312	0.75	1.38	1.29	1.11
27	−61.201249	13.134382	0.64	1.24	1.16	0.98
28	−61.19366	13.129567	0.44	1.03	0.96	0.80
29	−61.178734	13.138937	0.57	0.67	0.63	0.54
30	−61.154047	13.146989	0.39	0.23	0.22	0.21
31	−61.15914	13.149486	0.51	0.29	0.29	0.27
32	−61.146673	13.161864	0.43	0.19	0.19	0.20
Bequia	−61.230296	13.014004	0.45	0.05	0.06	0.16

volcano with around 6 wt% of water within magmas at 1100 K (Brazier et al., 1982; Heath et al., 1998). Besides these volcanological parameters, FPlume uses two turbulent air entrainment coefficients (the radial and the cross-flow air entrainment coefficients, α and β respectively) to describe the air mixing in the plume, which are critical for the MER assessment (Costa et al., 2016b; Suzuki and Koyaguchi, 2015).

Within FPlume, particle-particle aggregation is controlled by the presence of water from both magmatic and atmospheric origins (Costa et al., 2010; Folch et al., 2010, 2016). Ash aggregation effects on the plume transport are investigated through a comparative study that first neglects (hereinafter *None*) and, then accounts for aggregation processes making use of:

- i) *Cornell* scheme (hereinafter *Cornell*, based on Cornell et al., 1983). This parameterization assumes an effective aggregated class with a diameter d_{Agg} (or Φ_{Agg}) and density ρ_{Agg} , formed by 50% of particles with diameter 63–44 μm ash, 75% of 44–31 μm , and 90% of ash smaller than 31 μm ;
- ii) *Percentage* scheme (hereinafter *Percentage*, Sulpizio et al., 2012) assumes an effective aggregated class with a diameter d_{Agg} (or Φ_{Agg}) and density ρ_{Agg} , composed by depleting of a constant percentage each particle class involved in aggregation (i.e. classes characterized by primary particle diameter lower than d_{Agg} or greater than Φ_{Agg}). The constant percentage is inverted to best-fit the field deposit;
- iii) *Costa* scheme (Costa et al., 2010; Folch et al., 2010) considers wet aggregation under an effective aggregated class characterized by a diameter d_{Agg} (or Φ_{Agg}) and density ρ_{Agg} . *Costa* is based on two pre-calibrated parameters, the fractal exponent (D_f) and the aggregate settling velocity correction factor (ψ_e) related to aggregate porosity (Costa et al., 2010; Folch et al., 2016). This option represents a compromise between the full aggregation processes described by the Smoluchowski equation (Smoluchowski, 1917) and the need to reduce the bulk computational cost.

3.2. Meteorological model

FALL3D requires time-dependent wind fields and other meteorological variables such as air temperature and moisture over the computational domain. Here, we use the mesoscale WRF/ARW model (Skamarock et al., 2008) at two different spatial resolutions of 1 and 5 km to furnish meteorological data every 15 min. Initial and boundary conditions for WRF/ARW during the simulated period (i.e. from 25th April at 00 UTC to 29th April at 00 UCT) were obtained from the European Center for Medium-Range Weather Forecasts (ECMWF), ERA-Interim-Reanalysis branch (www.ecmwf.int) which provides 4-times daily data at 37 pressure levels (up to 1 mb) and 0.75° horizontal resolution. A nested strategy was adopted with inner domains at 5 and 1 km spatial resolution in order to investigate the role of meteorological model resolution in case of a short-lived eruption on complex steep terrains like St. Vincent Island.

3.3. TGSD estimation

Fig. 2 (bars) shows the TGSD estimated from 33 tephra deposits (Brazier et al., 1982, hereinafter Brazier TGSD), ranging from -2 to 8Φ with two modes at 1Φ and 4Φ referring to the coarse- and fine-grain sub-populations, respectively. The TGSD bi-modality was originally interpreted as a result of the lack of ground measurements beyond 36 km from the volcano (Brazier et al., 1982). Later, this was attributed by Brazier et al. (1983) to the premature fallout of fine ash deposited as aggregates. More recently, Costa et al. (2016a, 2017) showed how the presence of two different sub-populations within the TGSD is a common feature for most eruptions when they are properly sampled up to distal region. In any case, bi-modal granulometry features within the individual grain-size distributions on tephra deposits from proximal to distal

locations are a clear field signature of ash aggregation occurrence (Brazier et al., 1983; Durant et al., 2009). Starting from Brazier's TGSD estimation, we described the TGSD as the sum of two lognormal distributions (Fig. 2, bi-Gaussian in Φ , hereinafter bi-Gaussian distribution) and discretized the distribution each Φ -unit by using the following equation (Costa et al., 2016a, 2017):

$$f_{\text{bi-Gaussian}}(\Phi) = p \frac{1}{\sigma_1 \sqrt{2\pi}} e^{-\frac{(\Phi-\mu_1)^2}{2\sigma_1^2}} + (1-p) \frac{1}{\sigma_2 \sqrt{2\pi}} e^{-\frac{(\Phi-\mu_2)^2}{2\sigma_2^2}} \quad (1)$$

where Φ denotes particle diameters, p and $(1-p)$ are the fractions of each sub-population, μ_1 , μ_2 and σ_1 , σ_2 represent, respectively, the mean and standard deviation of the two Gaussian distributions in Φ -units. The best-fit parameters of the distribution, i.e. p , μ_1 , σ_1 , μ_2 , and σ_2 , are reported in Table 2. The Brazier TGSD was also described through the sum of two Weibull distributions (Fig. 2, bi-Weibull in Φ , hereinafter bi-Weibull distribution) and discretized each Φ -unit by using the following equation (Costa et al., 2016a, 2017):

$$f_{\text{bi-Weibull}}(d) = q \frac{1}{n_1 \frac{1}{\lambda_1} \Gamma\left(1 + \frac{1}{n_1}\right)} \frac{1}{\lambda_1} \left[\frac{d}{\lambda_1}\right]^{n_1} e^{-\frac{1}{\lambda_1} \left(\frac{d}{\lambda_1}\right)^{n_1}} + (1-q) \frac{1}{n_2 \frac{1}{\lambda_2} \Gamma\left(1 + \frac{1}{n_2}\right)} \frac{1}{\lambda_2} \left[\frac{d}{\lambda_2}\right]^{n_2} e^{-\frac{1}{\lambda_2} \left(\frac{d}{\lambda_2}\right)^{n_2}} \quad (2)$$

where, q and $(1-q)$ are the fraction of each sub-population, λ_1 , λ_2 , and n_1 , n_2 represent, respectively, the scale and shape parameters of the two distributions. The corresponding best-fit parameters (Costa et al., 2016a, 2017), i.e. q , λ_1 , n_1 , λ_2 and n_2 , are reported in Table 2.

FALL3D uses the input TGSD as discrete size bins. While the Brazier TGSD provides the field-based GSDs for each bin, the GSDs derived from both the bi-Gaussian and bi-Weibull distributions are estimated through the Eqs. (1) and (2), respectively, and reported in Table 3. Additionally, we assigned the mean density for each size bin accordingly to the simple parameterization of Bonadonna and Phillips (2003) for an andesitic magma.

3.4. Inverse problem-solving methodology

A set of FALL3D model runs was performed by exploring the ranges of the input parameters in Table 4 (see the Appendix A for the complementary description of the models and parameterization used). Optimal ESP values were obtained by best-fitting the observed loadings with the field measurements through the evaluation of the goodness-of-fit making use of different statistical parameters. The goodness-of-fit method considered the normalized Root Mean Square Error (i.e. $RMSE$) calculated using two different weights (i.e. $RMSE_1$ and $RMSE_2$) by the following equations:

$$RMSE_j = \sqrt{\sum_i^N w_j (Sim_i - Obs_i)^2} \quad (3)$$

where w_j refers to the weighting factors used to determine the $RMSE$. The index i corresponds to the i th sample over a set of N samples. The terms Obs_i and Sim_i are respectively the observed and simulated tephra loadings and:

$$w_{j=1} = \frac{1}{\sum_i^N Obs_i^2} \quad (4)$$

$$w_{j=2} = \frac{1}{N \times Obs_i^2} \quad (5)$$

These weights correspond to different assumptions on the error distribution (Costa et al., 2009). The $RMSE_1$ is calculated with w_1 and refers

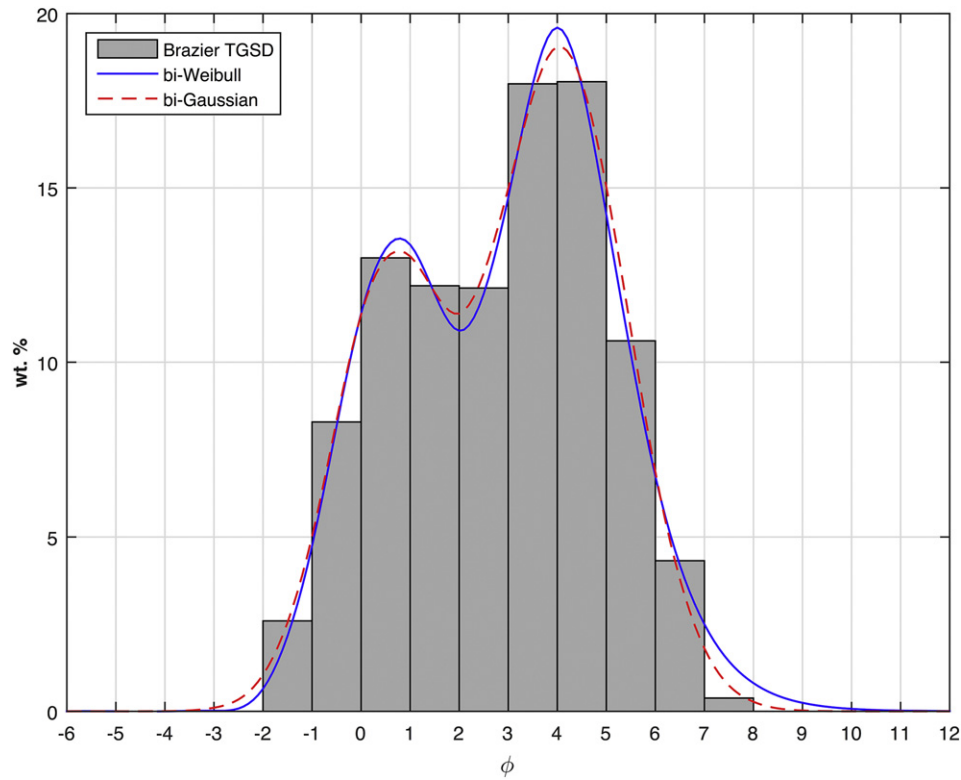


Fig. 2. Histogram shows the field-based TGSD (Brazier et al., 1982). The red dashed curve represents its best-fit with two lognormal distributions and the blue solid line with two Weibull distributions (Costa et al., 2016a, 2017). Analytical curve parameters are reported in Table 2.

to the case of a constant absolute error, whereas the $RMSE_2$ considers a constant relative error implying the proportional weighting factor w_2 (Folch et al., 2010). In addition to these $RMSE$ skills, we also computed the statistical indexes K (i.e. geometric average of the distribution) and k (i.e. geometric standard deviation of the distribution) introduced by Aida (1978):

$$K = \exp \left[\frac{1}{N} \sum_i^N \log \left(\frac{Obs_i}{Sim_i} \right) \right] \quad (6)$$

$$k = \exp \left[\sqrt{\frac{1}{N} \sum_i^N \log \left(\frac{Obs_i}{Sim_i} \right)^2 - \left(\frac{1}{N} \sum_i^N \log \left(\frac{Obs_i}{Sim_i} \right) \right)^2} \right] \quad (7)$$

Simulations are considered reliable when K lies between 0.95 and 1.05 (i.e. $\pm 5\%$ of the mass estimation). The optimal simulations (Table 5) are selected when k is minimized together with $RMSE_1$ and $RMSE_2$. Additionally, results of the simulations are chosen on the basis of the minimum

Table 2

Main parameters used to best-fit the Field TGSD (Brazier et al., 1982). For the lognormal distribution (bi-Gaussian), p is the coarse sub-population fraction; μ_1, μ_2 , are respectively the coarse- and fine-grained sub-populations means; σ_1, σ_2 are respectively the standard deviations of the coarse- and fine-grained sub-populations means. For the bi-Weibull distribution, q is the coarse sub-population fraction; λ_1, λ_2 , are respectively the scale parameters of the coarse- and fine-grained sub-populations means; n_1, n_2 are respectively the shape parameters of the coarse- and fine-grained sub-populations means (Costa et al., 2016a, 2017).

bi-Gaussian		bi-Weibull	
μ_1	0.557 ± 0.067	λ_1	0.269 ± 0.020
σ_1	1.146 ± 0.059	n_1	0.637 ± 0.039
μ_2	4.084 ± 0.049	λ_2	0.028 ± 0.001
σ_2	1.344 ± 0.045	n_2	0.875 ± 0.059
p	0.362 ± 0.020	q	0.495 ± 0.053

bias and the maximum correlation (Costa et al., 2009; Folch et al., 2010), where the normalized bias is calculated as (Folch et al., 2010):

$$Bias = \frac{\sum_i^N (Sim_i - Obs_i)}{\sum_i^N Obs_i} \quad (8)$$

For solving the inversion, we sampled at regular intervals through the ranges of the main parameters governing the tephra transport and sedimentation. Then, we refined the search using finer steps around the values giving the best goodness-of-fit. We started with the eruptive

Table 3

Grain-size distributions for the Brazier TGSD accompanied by the ones derived from the bi-Gaussian and bi-Weibull distributions (Fig. 2).

Diameter (Φ -unit)	Weight (%)		
	Brazier TGSD	bi-Gaussian TGSD	bi-Weibull TGSD
−6	0.00	0.00	0.00
−5	0.00	0.00	0.00
−4	0.00	0.00	0.00
−3	0.00	0.10	0.02
−2	2.59	1.05	0.65
−1	8.30	5.02	4.74
0	12.99	11.37	11.40
1	12.19	13.04	13.37
2	12.13	11.39	10.90
3	17.98	14.99	14.72
4	18.05	19.05	19.60
5	10.61	15.03	14.23
6	4.32	6.86	6.74
7	0.38	1.80	2.50
8	0.00	0.27	0.81
9	0.00	0.02	0.24
10	0.00	0.00	0.07
11	0.00	0.00	0.02
12	0.00	0.00	0.01

Table 4
Input parameter ranges explored within the simulations.

Input parameter	Explored range	
Column height (km a.v.) ^a	10	16
MER (kg/s) ^a	10 ⁴	10 ⁸
Exit velocity (m/s)	150	300
Exit temperature (K)	1000	1200
Exit water fraction (%) ^b	4.0	6.5
Cross-flow entrainment coefficient (β) ^c	0.3	1.0
Radial entrainment coefficient (α) ^c	0.1	0.15
Aggregate diameter (Φ -unit) ^d	0	2
Aggregate density (kg/m ³) ^d	100	800

^a The column height and MER are estimated using the FPlume model (Folch et al., 2016).

^b The magma exit water fraction is set accordingly to the literature (Brazier et al., 1982, 1983; Heath et al., 1998).

^c The entrainment coefficients (α and β) are set to a constant value (CONSTANT option in FPlume model, Folch et al., 2016).

^d Aggregation is investigated using the following schemes: *None* (i.e. no aggregation), *Cornell* (Cornell et al., 1983, modified), *Percentage* (Sulpizio et al., 2012) and *Costa* (Costa et al., 2010). The complementary values are reported in Table 5.

column height by exploring from 10 to 16 km above the vent. Through the relationship between the column height and the MER (Folch et al., 2016), column heights were obtained varying MERs from 10⁴ to 10⁸ kg/s. The exit velocity, temperature and water fraction are sampled from 150 to 300 m/s, 1000 to 1200 K and 4 to 6.5%, respectively. In addition to these ESPs, FPlume needs two entrainment coefficients (α and β), which were explored from 0.1 to 0.15 and from 0.3 to 1.0, respectively. Regarding the aggregation parameterization, the diameter (Φ_{Agg}) and density (ρ_{Agg}) of the aggregated class were chosen within the ranges 0 to 2 Φ , for Φ_{Agg} , and 100 to 800 kg/m³, for ρ_{Agg} .

4. Results

Here we present the results of the solution of the inverse problem together with sensitivity studies on tephra dispersal making use of: i) three different TGSD and, ii) the effects of different ash aggregation parameterizations. A sensitivity study on the meteorological model spatial resolution was also performed and is available in the supplementary material (Fig. S).

4.1. ESP estimation solving an inverse problem for the different TGSD

For the sake of clarity, the following section reports the use of the *Costa* aggregation scheme but all the optimal set of ESPs are summarized in Table 5 together with the statistical response. The interdependency of many of the input parameters implies that the reported optimal results are not unique (e.g. Anderson and Segall, 2013) and may differ with other ESP combinations (e.g. Connor and Connor, 2006; Scollo et al., 2008). The inversion procedure consists of running hundreds of simulations covering the ranges of the main parameters (Table 4) and choosing the combination that optimizes the tephra transport and sedimentation. To be concise, we reported in Fig. 3 the main parameter (i.e. column height) having substantial effect on the resulting tephra loadings and therefor on the best-fit agreement with the measured loadings. Fig. 3 summarizes the results in terms of $RMSE_1$, $RMSE_2$ and k showing how the goodness-of-fit is affected by varying pivotal parameters such as the column height (and the associated MER) with the *Costa* aggregation scheme. Sensitivity studies show that the effect of the column height (and associated MER) on k and $RMSEs$ is much more significant than on other parameters. As an example, the tephra loading appears to not be considerably affected varying the aggregate density. However, k is minimum for $\rho_{\text{Agg}} = 450$ kg/m³ for the Brazier and bi-Gaussian TGSDs and 350 kg/m³ for the bi-Weibull distribution.

The optimal simulations for each TGSD with the *Costa* scheme suggest an eruptive column height of 12 km a.v., a resulting Total Erupted Mass (TEM) of $\sim 2.5 \times 10^9$ kg, $\sim 2.4 \times 10^9$ kg, and $\sim 2.8 \times 10^9$ kg for the Brazier TGSD, bi-Gaussian and bi-Weibull distributions, respectively.

Table 5
Summary of the optimal ESP values with the statistical response for the three input TGSDs for the four-different aggregation schemes (i.e. *None*, *Cornell*, *Percentage* and *Costa*).

Brazier TGSD		Aggregation scheme			
Input parameter		<i>None</i>	<i>Cornell</i>	<i>Percentage</i>	<i>Costa</i>
Column height (km a.v.)		12	12	12	12
MER (kg/s)		6.8E+6	5.5E+6	7.1E+6	6.5E+6
Exit velocity (m/s)		250	250	250	250
Exit temperature (K)		1100	1100	1100	1100
Exit water fraction (%)		6	6	6	6
Cross-flow entrainment coefficient (β)		0.85	0.60	0.90	0.80
Radial entrainment coefficient (α)		0.13	0.13	0.13	0.13
Aggregate diameter (Φ -unit)		—	1.5	1.5	1.5
Aggregate density (kg/m ³)		—	450	450	450
Computed aggregate fraction (in wt%)		0.0	34.9	31.9	00.6
Statistical metric					
K	0.99	1.02	1.02	1.02	1.03
k	2.44	2.40	2.20	2.20	2.43
$RMSE_1$	0.85	0.80	0.84	0.84	0.83
$RMSE_2$	0.98	0.96	0.89	0.89	0.92
Bias	0.00	0.00	0.00	0.00	0.00
Correlation	0.60	0.50	0.60	0.60	0.60

bi-Gaussian TGSD		Aggregation scheme			
Input parameter		<i>None</i>	<i>Cornell</i>	<i>Percentage</i>	<i>Costa</i>
Column height (km a.v.)		12	12	12	12
MER (kg/s)		6.8E+6	5.6E+6	7.1E+6	6.6E+6
Exit velocity (m/s)		250	250	250	250
Exit temperature (K)		1100	1100	1100	1100
Exit water fraction (%)		6	6	6	6
Cross-flow entrainment coefficient (β)		0.85	0.60	0.90	0.80
Radial entrainment coefficient (α)		0.13	0.13	0.13	0.13
Aggregate diameter (Φ -unit)		—	1.5	1.5	1.5
Aggregate density (kg/m ³)		—	450	450	450
Computed aggregate fraction (in wt%)		0.0	41.1	34.7	2.2
Statistical metric					
K	1.01	1.01	1.00	1.00	1.05
k	2.46	2.42	2.23	2.23	2.39
$RMSE_1$	0.86	0.82	0.86	0.86	0.84
$RMSE_2$	0.94	0.98	0.91	0.91	0.89
Bias	0.00	0.00	0.00	0.00	0.00
Correlation	0.50	0.50	0.60	0.60	0.60

bi-Weibull TGSD		Aggregation scheme			
Input parameter		<i>None</i>	<i>Cornell</i>	<i>Percentage</i>	<i>Costa</i>
Column height (km a.v.)		12	12	12	12
MER (kg/s)		7.4E+6	6.6E+6	8.3E+6	7.4E+6
Exit velocity (m/s)		250	250	250	250
Exit temperature (K)		1100	1100	1100	1100
Exit water fraction (%)		6	6	6	6
Cross-flow entrainment coefficient (β)		0.95	0.80	1.00	0.95
Radial entrainment coefficient (α)		0.13	0.13	0.14	0.13
Aggregate diameter (Φ -unit)		—	1.5	1.5	1.5
Aggregate density (kg/m ³)		—	350	350	350
Computed aggregate fraction (in wt%)		0.0	42.1	34.9	22.3
Statistical metric					
K	0.95	0.98	1.00	1.00	1.02
k	2.45	2.27	2.09	2.09	2.18
$RMSE_1$	0.91	0.86	0.95	0.95	0.89
$RMSE_2$	1.03	0.94	0.93	0.93	0.89
Bias	0.00	0.00	0.00	0.00	0.00
Correlation	0.60	0.60	0.70	0.70	0.60

These values are consistent with the TEM provided by Brazier et al. (1982), i.e. $\sim 9.6 \times 10^8$ kg, which is $\sim 40\%$ lower than our simulation results. Considering a constant MER through the 6 min of the eruption, the corresponding MERs for each distribution are of $\sim 6.5 \times 10^6$ kg/s, $\sim 6.6 \times 10^6$ kg/s, and $\sim 7.8 \times 10^6$ kg/s, respectively. Regarding the plume air entrainment coefficients, the best-fit values for this short-lived eruption of La Soufrière St. Vincent volcano give a radial entrainment coefficient α of 0.13 and a cross-flow entrainment coefficient β of 0.95, which are within the typical ranges (Costa et al., 2016b).

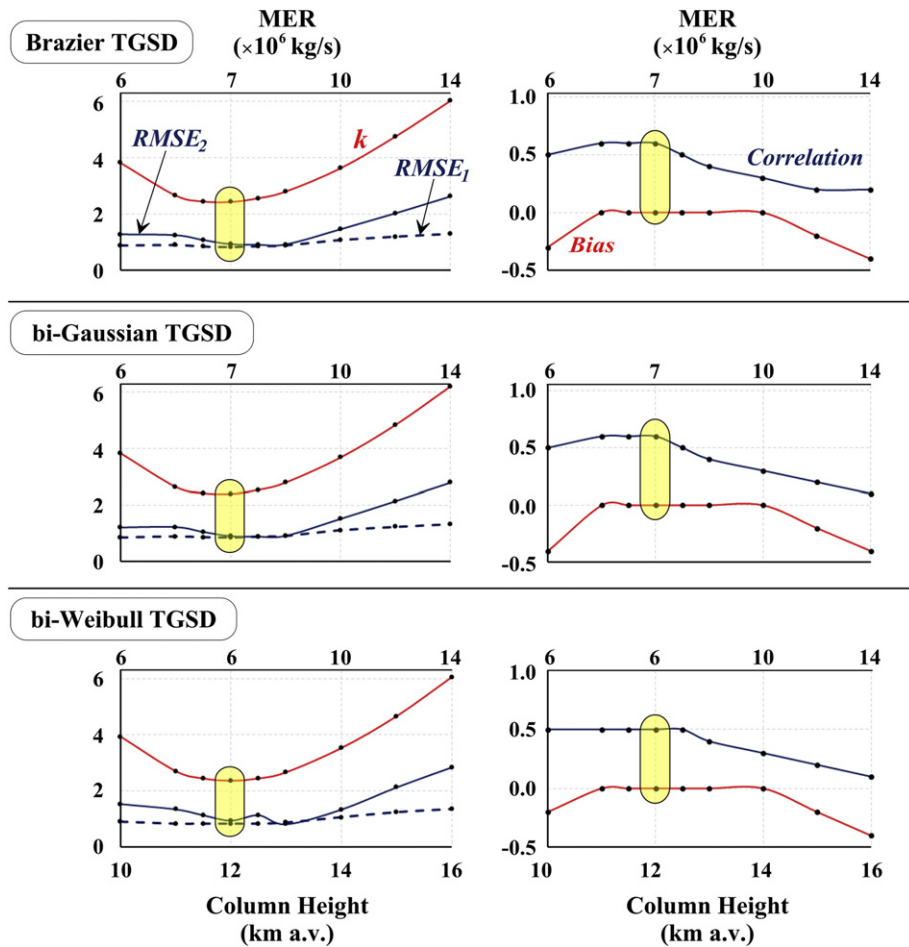


Fig. 3. Summary of the procedure used to solve the inverse problem showing the statistical indices ($RMSE_1$, $RMSE_2$ and k , Bias and Correlation) variations as function of total column height (and associate MER) for the three input TGSDs.

The bi-Weibull distribution combined with the *Costa* scheme give statistical indexes of $K = 1.02$ and $k = 2.18$ for the optimal simulation, whereas both the $RMSE_1$ and $RMSE_2$ are calculated at ~ 0.89 (see Table 5 for a full description of the results). These values indicate an error associated with the ESP estimation similar to the uncertainty associated with other classical methods (Bonadonna and Costa, 2012, 2013; Bonadonna et al., 2015). Fig. 4a shows the comparison between the measured and the computed tephra loading values on a logarithmical scale at the 31 considered locations (Fig. 1). Overall, the best simulations indicate that 94% of the tracked samples fall between 1/5- and 5-times the observed values and 6% (the 2 most proximal samples) fall nearby the 1/10- and 10-times. Fig. 4a also compares the results obtained with the bi-Weibull distribution accounting for aggregation using the *Costa* scheme and no aggregation. It also displays the best simulations for the bi-Gaussian distribution and the Brazier TGSD with the *Costa* scheme. Overall, Fig. 4a illustrates how accounting for aggregation processes improves those neglecting it. Table 5 summarizes the goodness-of-fit results obtained for the three TGSD employed in combination with the different aggregation schemes. The table shows similar $RMSE_1$, $RMSE_2$ and k index values, although obtained through different parameterizations. This reflects the convergence of the simulation to best-fit the field measurements. However, despite this similarity, Fig. 4a suggests considerable differences associated with the tephra loading at the Bequia location (0.45 kg/m^2). The simulations under aggregation improve the fitting almost by a factor 6. The 31 different computed loadings can be compared with the field measurements in Table 1.

In addition to the best-fit tephra loadings, the observed accumulation rate (in $\text{kg/m}^2/\text{min}$) made at the Belmont Observatory (label 6 in

Fig. 1a) is also compared against the modelled rate (Fig. 4b). The dashed line indicates a maximum accumulation rate of $\sim 3.8 \text{ kg/m}^2/\text{min}$ around 25 min after the eruption start. This trend is reproduced by the model but required a 15-minute time shift on the meteorological database to capture the proper accumulation-loading rate, which is attributed to a meteorological model phase error that does not represent correctly the meteorological fields. From a computational point of view, this operation is done by shifting the eruption start by -15 min. In this case, a maximum of $\sim 1.8 \text{ kg/m}^2/\text{min}$, which is of the same order of the measured value, is obtained around 25 min after the eruption start.

Fig. 5 shows the tephra loading map for the optimal simulation, i.e. with the bi-Weibull distribution and the *Costa* scheme. Besides the tephra blanket covering most of the St. Vincent and Bequia islands, the map presents an area with an expanded maximum spreading south-eastwards (i.e. following the load limit of 2 kg/m^2), which is associated with the aggregates fallout (see the time-series Animation Loading in the supplementary material). In this case, ash aggregation is contributing to $\sim 22.3\%$ of the tephra fallout deposit. A time-series animation of the computed aggregate deposition is available in the supplementary material (see Animation Aggregate Loading). Further details on the effects of ash aggregation scheme on simulation results are described in the following Section 4.2.

4.2. Sensitivity to parameterizations of ash aggregation

For the sake of clarity, ash aggregation results are presented in subsections referring to the use of a TGSD (i.e. Brazier TGSD, bi-Gaussian and bi-Weibull distributions respectively). For each case, we show the tephra loading (Fig. 6) and aggregate loading maps (Fig. 7). The columns

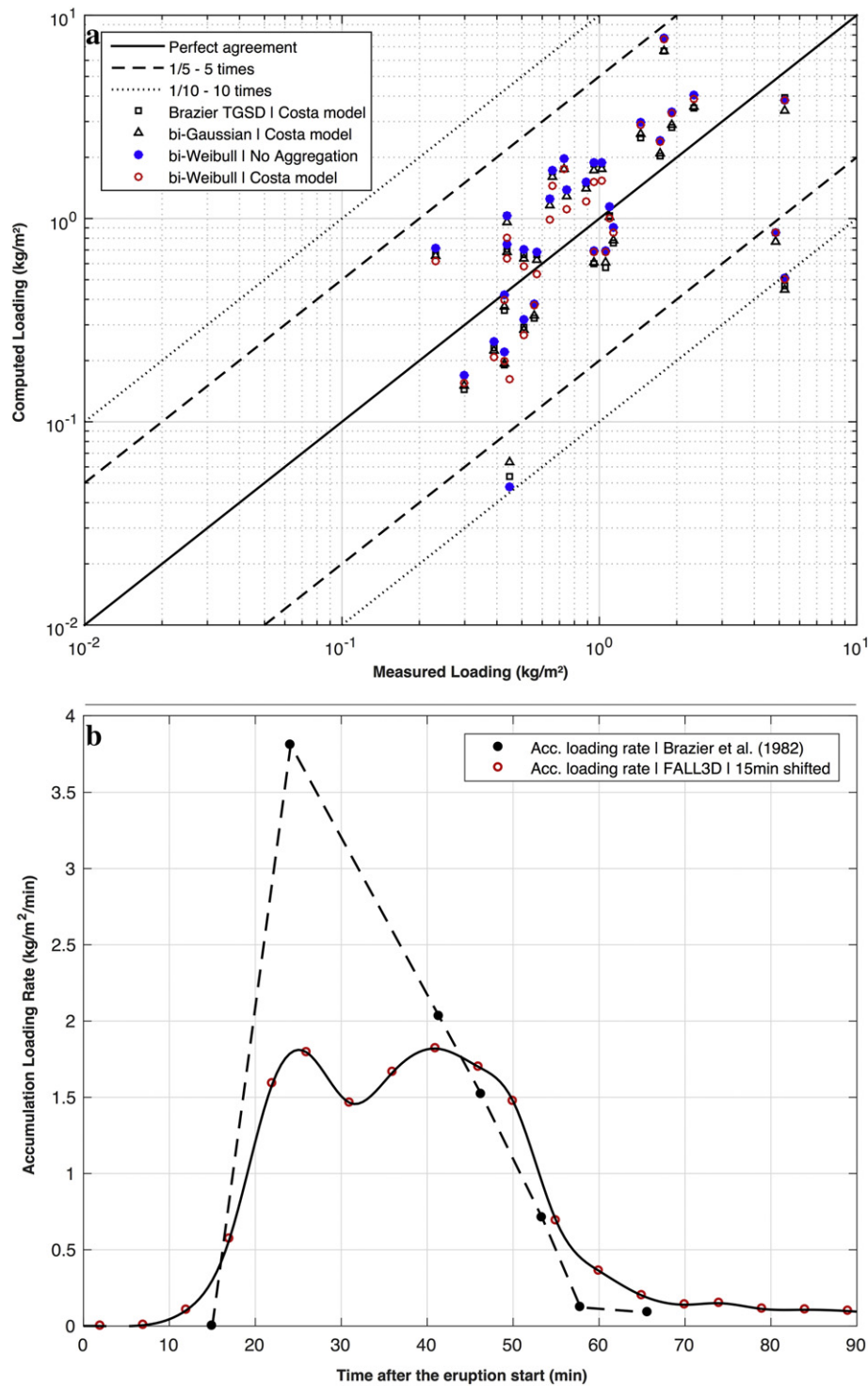


Fig. 4. a Comparison between the observed ground loadings and its best-fit computed values for the 31 sample locations (loading details in Table 1). Reported results refer to the use of the Costa scheme (Costa et al., 2010) with the Field TGSD (squares), the bi-Gaussian (triangles) and the bi-Weibull distributions (unfilled red circles). Blue spheres stand for the bi-Weibull distribution neglecting aggregation (i.e. *None* scheme). b Comparison of the tephra accumulation loading rate from field-based observations (Brazier et al., 1982) at Belmont Observatory (black dots with dashed line) with the computed rate (red dots with solid line).

in Figs. 6 and 7 display the results for each TGSD while rows illustrate the different aggregation schemes (i.e. *None*, *Cornell*, *Percentage* and *Costa*). Overall, Fig. 6 highlights the effect of each aggregation parameterization on the tephra transport and deposition (the corresponding aggregate mass fractions are regrouped in Table 5). Regarding the aggregated class, simulation results give optimal values for the effective aggregate diameter of 0.35 mm ($\Phi_{\text{Agg}} = 1.5$). The best density value is obtained at 450, 450 and 350 kg/m³ for the Brazier TGSD, bi-Gaussian

and bi-Weibull distributions respectively. The fractal exponent (D_f) required by the Costa scheme is set at 3. The optimal input aggregate fraction needed by the *Percentage* scheme is obtained at 50% to the fines (~35% for the TGSD).

4.2.1. Ash aggregation results for the Brazier TGSD

Tephra loading maps resulting from the use of the Brazier TGSD (left column in Fig. 6) show the effect of the four aggregation scheme on the

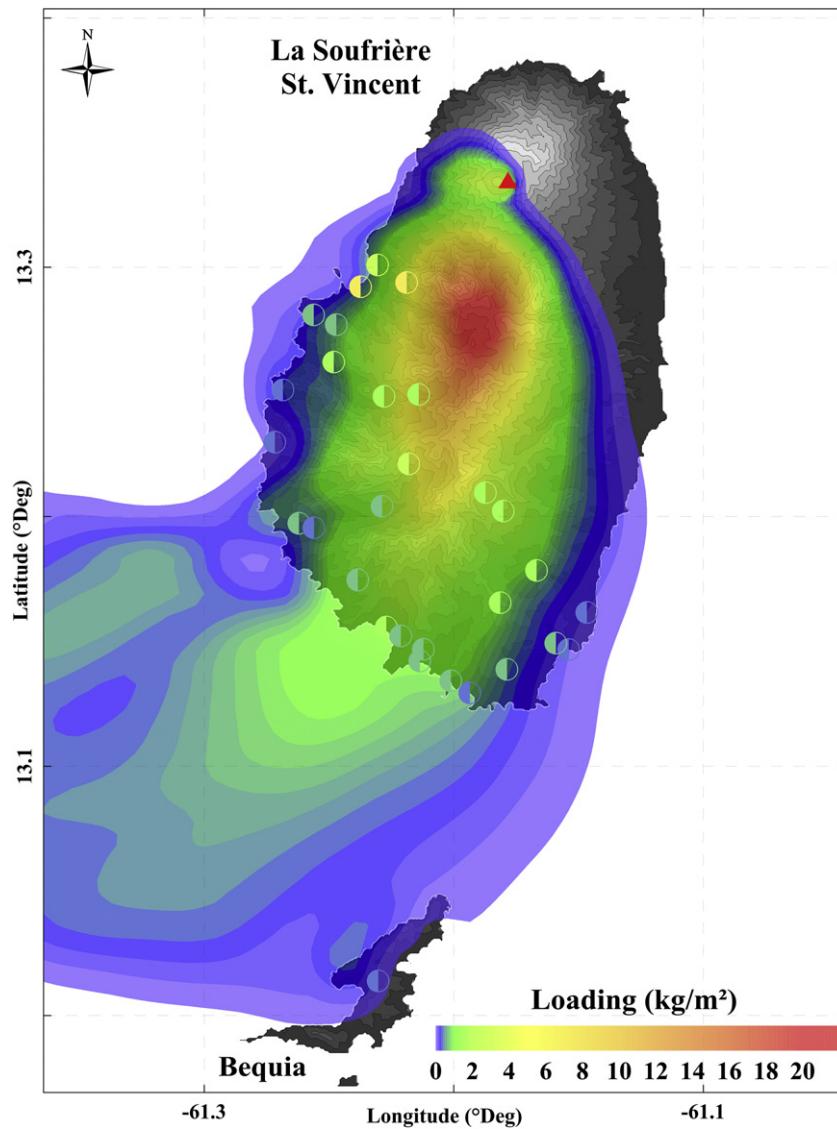


Fig. 5. Best tephra loading map resulting from the use of the bi-Weibull distribution and the *Costa* scheme. Color bar and samples color scale are adjusted to match when computed loadings lie within the observed range value. The figure is generated using the Kriging gridding method described in Yang et al. (2004).

deposit. Results give computed aggregate mass fractions from 0% (assuming no aggregation) to ~35%. Although the maps show similar tephra deposits for *None*, *Cornell*, *Percentage* and *Costa* schemes, the aggregate mass fraction given by *Costa* is very low (~0.6%), suggesting almost no presence of aggregates on the deposit. *Cornell* and *Percentage* schemes have a similar much higher aggregate fraction (~35% and ~32%, respectively), thus improving the reconstruction of the deposit at Bequia. *None* and *Costa* methods are not able to capture the field measurement at Bequia Island but *Cornell* and *Percentage* schemes do. Fig. 7 (left column) presents the computed aggregate-loadings and shows the different contributions between the aggregation scheme.

4.2.2. Ash aggregation results for the bi-Gaussian TGSD

Tephra loading maps associated with the use of the bi-Gaussian distribution are summarized in Fig. 6 (central column). The estimated aggregate mass fraction ranges from 0% to ~41%. As observed in Section 4.2.1, *Costa* results in a low aggregate fraction (~2.2%), explaining the similarity between the maps for *None* and *Costa*. Then, *Cornell* and *Percentage* schemes indicate similar but greater fractions (~41% and ~35%, respectively), increasing the deposit at Bequia visible on Fig. 6. Again, *None* and *Costa* schemes are not able to capture the

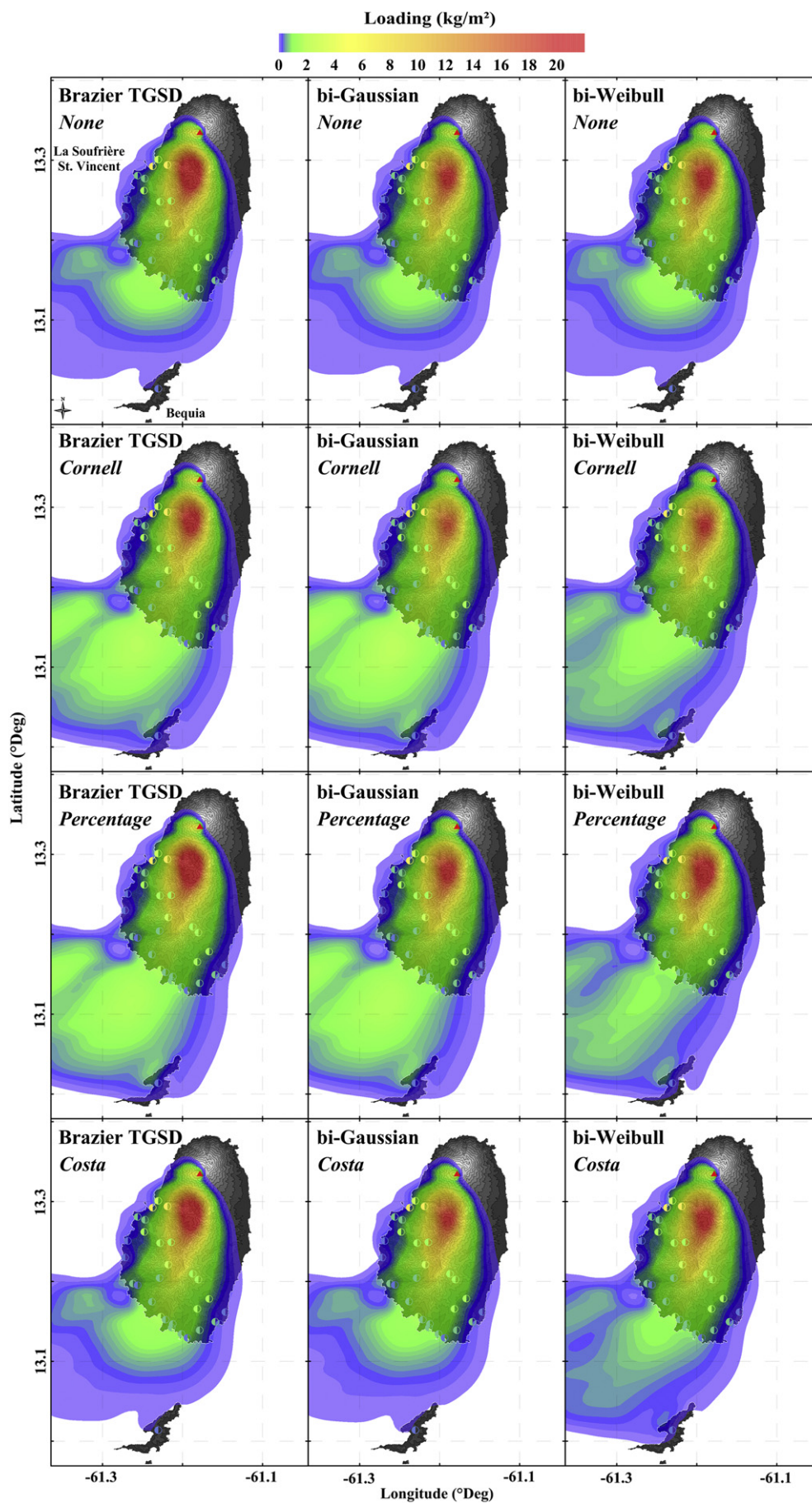
field measurement in Bequia Island, whereas *Cornell* and *Percentage* schemes show a better agreement (Fig. 7, central column).

4.2.3. Ash aggregation results for the bi-Weibull TGSD

Tephra loading maps associated with the use of the bi-Weibull distribution are summarized in Fig. 6 (right column). The computed aggregate mass fractions range from 0% to ~42%. The use of the bi-Weibull distribution gives a different behavior with respect to the Sections 4.2.1 and 4.2.2. For this particular case, the *Cornell*, *Percentage* and *Costa* schemes show very similar tephra loadings together with similar aggregate fractions (~42%, ~35% and ~22%, respectively). In particular, the statistical analysis (i.e. RMSEs, *K*, *k*, bias and correlation) in Table 5 shows the best performance for the *Costa* and *Percentage* schemes. The agreement is also visible through the simulated tephra deposits, capable to capture the loadings measured in Bequia. Fig. 7 (right column) illustrates the aggregate loading maps, which are very similar in this case.

5. Discussion

This study aims at reconstructing the main features of the 26th April 1979 eruption at La Soufrière St. Vincent volcano, constraining ESPs and



ash aggregation processes using the FALL3D tephra dispersal model together with a 1 km resolution mesoscale meteorological model. Simulations are validated against all available data in terms of tephra loading, grain-size distribution and plume observations. This study allows us to gain insight into aggregation parameterizations as well as on the control of the driving meteorology on these processes.

Considering the proximal area (i.e. < 10 km from the vent), the deposit mapped may have fallen from the rising column rather than from the downwind cloud. Although the gravitational spreading (Costa et al., 2013) is taken into account by the FALL3D code, the resulting tephra loadings may show significant discrepancies due to the high unstable plume conditions and complex multiphase processes near the vent (e.g. Manzella et al., 2015; Cerminara et al., 2016; Del Bello et al., 2017). Substantial differences between the computed and measured loadings were observed for the two closest points from the source (labels 1 and 2 in Fig. 1). Because the tephra dispersal model limitations at very proximal region, we did not consider these two points. The eruptive column is described by the FPlume model which, for each grain-size bin (characterized by particle size, density, and shape), provides the mass flow over the entire range of elevations. Then, making use of the meteorological database FALL3D computes the transport and deposition for each grid node (i.e. longitudes and latitudes) and the elevation layers.

Amongst the main ESPs, the input TGSD plays a pivotal control on tephra deposition (Costa et al., 2016a) and aggregation (Folch et al., 2016), but is particularly difficult to estimate, especially for the fine ash tail (Costa et al., 2016a and references therein). For this reason, we carried out a sensitivity study on the TGSD by considering different estimations (Section 3.3). Results associated with the TGSDs demonstrate ash aggregation to be highly dependent on the TGSD tail description (i.e. $\Phi > 5$), but also on the aggregation scheme (Table 5). While Brazier TGSD has only ~15.3% of fine ash (bars in Fig. 2) the bi-Gaussian distribution contains ~24.0% (red dashed line in Fig. 2), and the bi-Weibull distribution ~24.6% (blue solid line in Fig. 2). In our context, fine ash enrichment implies a greater aggregation contribution on the medial bulk tephra fallout, which is illustrated in Fig. 6. This figure shows (from left to right) that enriching in fine ash reproduces slightly better the tephra dispersal and deposition independently from the aggregation scheme used. This is observable by the extent of the computed tephra fallout towards the Bequia Island. However, neglecting aggregation (top panels in Fig. 6) returns identical results regardless of the TGSD used, highlighting the non-uniqueness parameterization to best-fit the field observations. These results illustrate how important it is to consider aggregation together with the correct fine ash tail description of the distribution. In particular, results from the Costa parameterization give aggregate mass fractions from ~0.6–2.2% (i.e. for Brazier TGSD and bi-Gaussian distribution, respectively) to ~22.3% (i.e. for the bi-Weibull distribution). These values indicate a strong dependency on TGSD estimation as indicated in Figs. 6 and 7. The Percentage (and Cornell) scheme (detailed in Section 3.1) indicates more stable loadings through the three TGSD and show a good agreement with the observed deposit. However, the Percentage scheme has a slightly better performance (Table 5) with respect to the optimal results obtained for the bi-Weibull TGSD with the Costa parameterization. The Percentage scheme, which has the lowest k and highest correlation, suggests similar ESPs than the other schemes but aggregate mass fraction of ~35% (Table 5). Nonetheless, the remarkable result shown by Fig. 6 is the non-uniqueness solution to best reproduce the field deposit, which is attributed to the interdependency of the main parameters that lead to a set of reliable parameterizations.

Fig. 8 brings together the four GSD displayed in Brazier et al. (1982) for samples 3, 6, 25, and Bequia, respectively (located at 6, 10, 21, and 36 km from the vent; Fig. 1a). For the sake of clarity, Fig. 8 reports GSDs estimated with the bi-Weibull distribution. The paragraph refers to the use of

the Costa aggregation scheme. The figure shows the computed and measured GSD (hereinafter Field GSD) for all the diameter bins (i.e. $-4 < \Phi < 8$). Field GSDs present coarse and fine sub-populations. On one hand, the coarse sub-population peaks at $\Phi = 0$ (sample 3), $\Phi = 1$ (samples 6 and 25) and at $\Phi = 2$ (sample Bequia) representing tephra settling as free particles. The corresponding computed modes and variances of these GSDs are in agreement with the field observations. On the other hand, the fine sub-population, which is composed of particles that deposited as aggregates (mostly destroyed when impacting the ground, thereby releasing fine ash in the deposit) was not properly simulated, especially at proximal locations reflecting the difficulty to accurately describe the coarse tail of the TGSD without a proper sampling of the proximal area (Andronico et al., 2014; Spanu et al., 2016). Discrepancies for the fine sub-population can be explained by the ash aggregation schemes that consider only one single effective aggregate class rather than a distribution of aggregates with different sizes and densities (Mastin et al., 2016).

The best-case simulation results obtained for an effective aggregate diameter of $\Phi_{\text{Agg}} = 1.5$ and a density of 350 kg/m^3 using the Costa scheme with a bi-Weibull TGSD indicate aggregate fractions of ~0.1%, ~0.4%, ~5.8% and ~78.2%, respectively, for the samples 3, 6, 25 and Bequia (i.e. Agg class on each panel in Fig. 8). These values can be compared with data from the relative Field GSDs, summing the measured mass fractions corresponding to the particle classes considered to settle as aggregates. The sum concerns the empty classes for None aggregation (Fig. 8), i.e. $\Phi \geq 3$ for sample 3, 6, and 25 and $\Phi \geq 4$ for the Bequia sample. The resulting sums give ~68.0%, ~56.0%, ~61.1% and ~43.6%, respectively (Agg class in Fig. 8). From a computational point of view, these latter fractions would be assigned, at least partially, in the aggregate class. While the values associated with the samples 3, 6 and 25 are not in agreement with the simulations, the performance for the Bequia is better.

The optimal simulation performed with the bi-Weibull distribution and the Costa scheme predicts an aggregate fraction of ~22.3%, contributing to the tephra deposit with ~0.5 kg/m^2 as maximum. The time-series of the sedimentation associated with the effective aggregated class can be used to identify the area impacted by the deposition of aggregates, which is located south-westwards from the main island and over the ocean (see Animation Aggregate Loading in the Supplementary material). These results agree with the observation of a bi-modal grain-size distribution as well as a secondary thickening in the tephra fallout described in Brazier et al. (1983), and more recently in Mastin et al. (2016) for Mount St. Helens (18th May 1980).

Fig. 8 highlights also the effect of air moisture on tephra dispersal and deposition by comparing GSDs obtained with the Costa scheme. Samples 3, 6 and 25 indicate a weak effect of the air moisture on the deposits, which is consistent with the local atmospheric conditions reported in Brazier et al. (1982) together with the phreatomagmatic feature of the eruption (Shepherd and Sigurdsson, 1982). In contrast, effect of air moisture is significant for the Bequia deposit (bottom right panel in Fig. 8). While the best results in Fig. 5 are obtained considering air moisture (~22.3% of aggregation), this fraction drops to ~0.8% when assuming only dry entrained air in the atmosphere. This indicates that atmospheric moisture significantly contributed to ash aggregation processes for the 26th April 1979 eruption. This also highlights the model sensitivity to air moisture, especially in tropical zones.

6. Conclusion

On 26th April 1979, a short-lived explosive eruption occurred at La Soufrière St. Vincent volcano generating an eruptive plume that raised about 13 km above the vent. Tephra dispersal was mainly governed by a wind blowing southwards, allowing tephra samples to be collected at 33 locations from the vent up to Bequia Island at 36 km southwards.

Fig. 6. Overview of the tephra loading maps obtained for the three input TGSDs together with the four aggregation schemes (i.e. None, Cornell, Percentage and Costa). The details are reported in Table 5. Color bar and samples color scale are adjusted to match when the computed loadings lie within the observed range value. The figure is generated using the Kriging gridding method described in Yang et al. (2004).

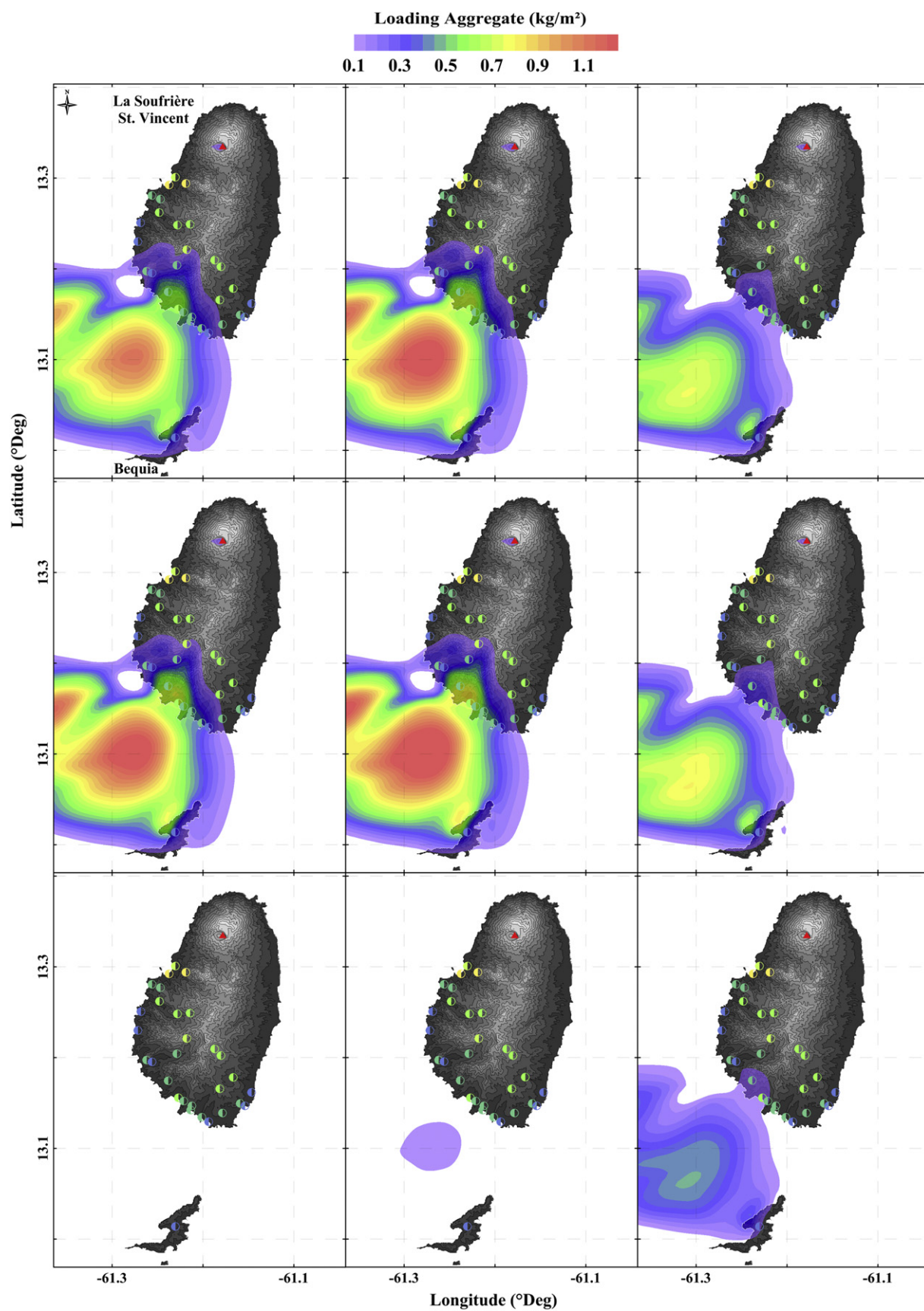


Fig. 7. Overview of the aggregate loading maps obtained for the three explored TGSDs and the four aggregation schemes (i.e. *None*, *Cornell*, *Percentage* and *Costa*). The details are reported in Table 5. Color bar and samples color scale are adjusted to match when the computed loadings lie within the observed range value. The figure is generated using the Kriging gridding method described in Yang et al. (2004).

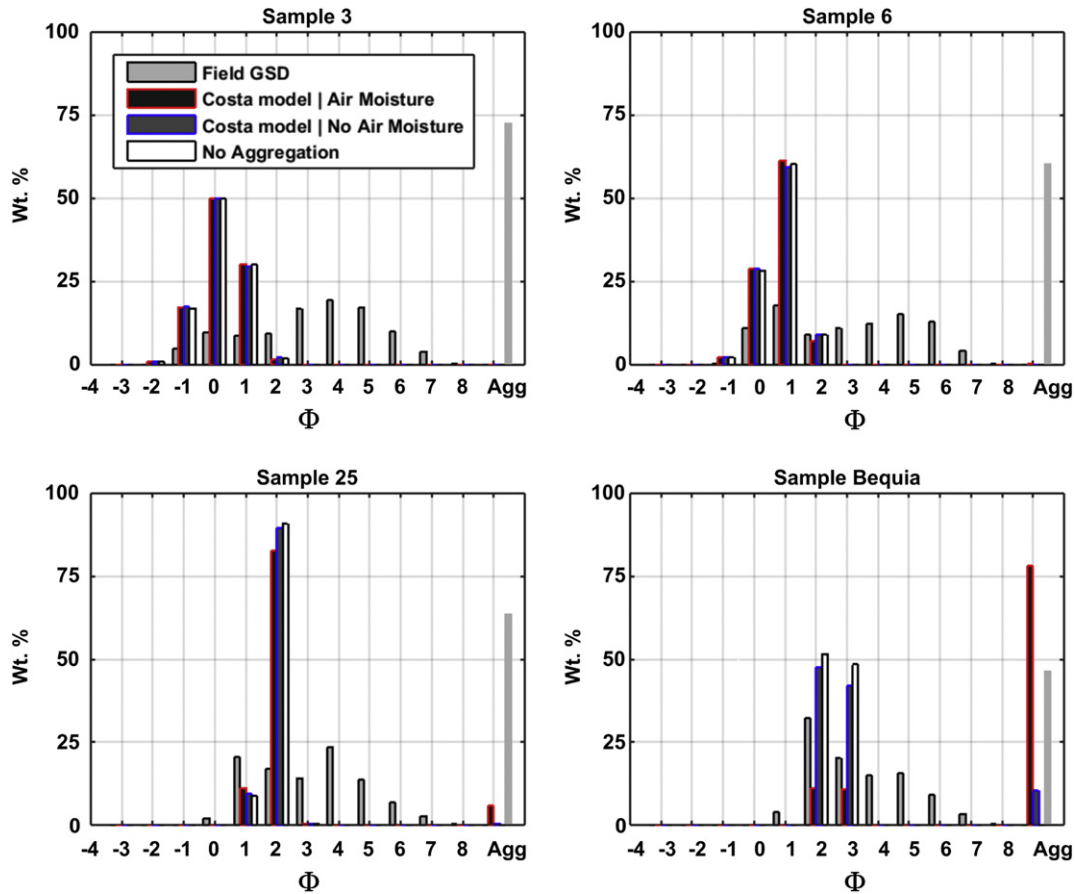


Fig. 8. Comparison of the Field GSD (i.e. labels 3, 6, 25 and Bequia) provided by Brazier et al. (1982) with the corresponding GSD calculated by FALL3D. Light grey bars represent the sum of the fine particle classes assumed falling as aggregates.

Field measurements were used to estimate Eruption Source Parameters (ESP). A previously estimated TGSD (Brazier et al., 1982) was complemented with both the sum of two lognormal and the sum of two Weibull distributions. Starting from these three input TGSDs, we best-fitted all the available data including tephra loading, grain-size distribution and plume observations. The effect of ash aggregation was also investigated by comparing three aggregation schemes with simulations neglecting aggregation phenomena. In order to better reconstruct the main eruption features, several hundreds of simulations were run with aggregation under wet conditions. The optimal results obtained using the FALL3D tephra dispersal model were selected through a goodness-of-fit method. These indicate a column height of ~12 km above the vent, a mean Mass Eruption Rate of $\sim 7.8 \times 10^6$ kg/s, and a Total Erupted Mass of $\sim 2.8 \times 10^9$ kg obtained for an eruption duration of 6 min. Best results suggest an estimation of ~22% for the fine ash fraction involved in aggregation processes. This work highlights the need for further field-based aggregation studies to better characterize the aggregation processes.

Acknowledgements

This work is supported by the FP 7 Marie Curie Actions Framework “FP7-PEOPLE-2013-ITN”, funding the Marie Curie Initial Training Network VERTIGO project (grant agreement number 607905). Meteorological data were provided by European Center for Medium-Range Weather Forecasts (ECMWF). WRF simulations were carried out at the MareNostrum-III Supercomputer (BSC-CBS, Barcelona, Spain). The DEM was provided by the SRTM90 platform (Jarvis et al., 2008). We thank Larry Mastin and the Editor Joan Martí for providing constructive comments which helped to improve the clarity and the quality of the manuscript.

Appendix A. Appendix

This section displays the others parameters and models used to run the simulations.

Parameters and models	
Time meteo domain	From 25/04 to 28/04/1979
Grid: bottom left (Longitude / Latitude)	-61.31 / -12.93
Grid: top right (Longitude / Latitude)	-61.08 / 13.40
Time step meteo data (min)	30
Grid nodes: (Longitude / Latitude)	70 / 101
Altitude layers (500 m step)	From 0 to 14500
Vent coordinates: (Longitude / Latitude)	-61.180743 / 13.333557
Vent elevation (m)	1220
Eruption duration (sec)	370
Eruption column model	FPlume ^a
Terminal velocity model	Ganser ^b
Vertical turbulence model	Similarity ^c
Horizontal turbulence model	RAMS ^d
RAMS C _s	0.3
Wet deposition	No

^a The eruption column model used is based on the Buoyant Plume Theory (BPT) as described in Folch et al. (2016).

^b The semi-empirical parameterization for the terminal settling velocity calculation is done through the Ganser option as described in Ganser (1993).

^c The vertical component of the eddy diffusivity tensor, K_z , is estimated using the Similarity option as in Costa et al. (2006) and Ulke (2000).

^d The horizontal component of the eddy diffusivity tensor, K_h , is evaluated as in Pielke et al. (1992) by the RAMS option.

Appendix B. Supplementary data

Supplementary data to this article can be found online at <https://doi.org/10.1016/j.jvolgeores.2017.09.012>.

References

- Aida, I., 1978. Reliability of a tsunami source model derived from fault parameters. *J. Phys. Earth* 26, 57–73.
- Anderson, K., Segall, P., 2013. Bayesian inversion of data from effusive volcanic eruptions using physics-based models: application to Mount St. Helens 2004–2008. *J. Geophys. Res. Solid Earth* 118 (5):2017–2037. <https://doi.org/10.1002/jgrb.50169>.
- Andronico, D., Scollo, S., Cristaldi, A., Lo Castro, M.D., 2014. Representivity of incompletely sampled fall deposits in estimating eruption source parameters: a test using the 12–13 January 2011 lava fountain deposit from Mt. Etna volcano, Italy. *Bull. Volcanol.* 76 (861). <https://doi.org/10.1007/s00445-014-0861-3>.
- Bonadonna, C., Costa, A., 2012. Estimating the volume of tephra deposits: a new simple strategy. *Geology* 40:415–418. <https://doi.org/10.1130/G32769.1>.
- Bonadonna, C., Costa, A., 2013. Plume height, volume, and classification of explosive volcanic eruptions based on the Weibull function. *Bull. Volcanol.* 75 (8):742. <https://doi.org/10.1007/s00445-013-0742-1>.
- Bonadonna, C., Phillips, J.C., 2003. Sedimentation from strong volcanic plumes. *J. Geophys. Res.* 108 (B7):2340. <https://doi.org/10.1029/2002JB002034>.
- Bonadonna, C., Biass, S., Costa, A., 2015. Physical characterization of explosive volcanic eruptions based on tephra deposits: propagation of uncertainties and sensitivity analysis. *J. Volcanol. Geotherm. Res.* 296:80–100. <https://doi.org/10.1016/j.jvolgeores.2015.03.009>.
- Brazier, S., Davis, A.N., Sigurdsson, H., Sparks, R.S.J., 1982. Fall-out and deposition of volcanic ash during the 1979 explosive eruption of the Soufriere of St. Vincent. *J. Volcanol. Geotherm. Res.* 14 (3–4):335–359. [https://doi.org/10.1016/0377-0273\(82\)90069-5](https://doi.org/10.1016/0377-0273(82)90069-5).
- Brazier, S., Sparks, R.S.J., Carey, S.N., Sigurdsson, H., Westgate, J.A., 1983. Bimodal distribution and secondary thickening in air-fall ash layers. *Nature* 301.
- Brown, R.J., Bonadonna, C., Durant, A.J., 2012. A review of volcanic ash aggregation. *Phys. Chem. Earth A/B/C* 45–46:65–78. <https://doi.org/10.1016/j.pce.2011.11.001>.
- Cerminara, M., Esposito Ongaro, T., Neri, A., 2016. Large Eddy Simulation of gas-particle kinetic decoupling and turbulent entrainment in volcanic plumes. *J. Volcanol. Geoth. Res.* 326:143–171. <https://doi.org/10.1016/j.jvolgeores.2016.06.018>.
- Connor, L.J., Connor, C.B., 2006. Inversion is the key to dispersion: understanding eruption dynamics by inverting tephra fallout. *Statistics in Volcanology*. 1, p. 241242.
- Cornell, W., Carey, S., Sigurdsson, H., 1983. Computer simulation of transport and deposition of Campanian Y-5 ash. *J. Volcanol. Geotherm. Res.* 17:89–109. [https://doi.org/10.1016/0377-0273\(83\)90063-X](https://doi.org/10.1016/0377-0273(83)90063-X).
- Costa, A., Macedonio, G., Folch, A., 2006. A three-dimensional Eulerian model for transport and deposition of volcanic ashes. *Earth Planet. Sci. Lett.* 241:634–647. <https://doi.org/10.1016/j.epsl.2005.11.019>.
- Costa, A., Dell'Erba, F., Di Vito, M.A., Isaia, R., Macedonio, G., Orsi, G., Pfeiffer, T., 2009. Tephra fallout hazard assessment at the Campi Flegrei caldera (Italy). *Bull. Volcanol.* 71:259–273. <https://doi.org/10.1007/s00445-008-0220-3>.
- Costa, A., Folch, A., Macedonio, G., 2010. A model for wet aggregation of ash particles in volcanic plumes and clouds: 1. Theoretical formulation. *J. Geophys. Res.* 115, B09201. <https://doi.org/10.1029/2009JB007175>.
- Costa, A., Folch, A., Macedonio, G., 2013. Density-driven transport in the umbrella region of the volcanic clouds: implications for tephra dispersion models. *Geophys. Res. Lett.* 40:1–5. <https://doi.org/10.1002/grl.50942>.
- Costa, A., Pioli, L., Bonadonna, C., 2016a. Assessing tephra total grain-size distribution: insights from field data analysis. *Earth Planet. Sci. Lett.* 443, 90–107.
- Costa, A., Suzuki, Y.J., Cerminara, M., Devenish, B., Esposito Ongaro, T., Herzog, M., Van Eaton, A., Denby, L.C., Bursik, M., de Michieli Vitturi, M., Engwell, S., Neri, A., Barsotti, S., Folch, A., Macedonio, G., Girault, F., Carazzo, G., Tait, S., Kaminski, E., Mastin, L., Woodhouse, M., Phillips, J.C., Hogg, A.J., Degruyter, W.J., Bonadonna, C., 2016b. Results of the eruption column model inter-comparison study. *J. Volcanol. Geotherm. Res.* <https://doi.org/10.1016/j.jvolgeores.2016.01.017>.
- Costa, A., Pioli, L., Bonadonna, C., 2017. Corrigendum to “assessing tephra total grain-size distribution: insights from field data analysis”. [*Earth and Planetary Sci. Lett.* 443, 90–107, 2016a]. *Earth Planet. Sci. Lett.* <https://doi.org/10.1016/j.epsl.2017.03.003>.
- Del Bello, E., Taddeucci, J., de Michieli Vitturi, M., Scarlato, P., Andronico, D., Scollo, S., Kueppers, U., Ricci, T., 2017. Effect of particle volume fraction on the settling velocity of volcanic ash particles: insights from joint experimental and numerical simulations. *Nature - Sci. Rep.* 6:39620. <https://doi.org/10.1038/srep39620>.
- Durant, A.J., Rose, W.I., Sarna-Wojcicki, A.M., Carey, S., Volentik, A.C.M., 2009. Hydrometeor-enhanced tephra sedimentation: constraints from the 18 May 1980 eruption of Mount St. Helens. *J. Geophys. Res.* 114, B03204. <https://doi.org/10.1029/2008JB005756>.
- Folch, A., Costa, A., Macedonio, G., 2009. FALL3D: a computational model for transport and deposition of volcanic ash. *Comput. Geosci.* 35:1334–1342. <https://doi.org/10.1016/j.cageo.2008.08.008>.
- Folch, A., Costa, A., Durant, A., Macedonio, G., 2010. A model for wet aggregation of ash particles in volcanic plumes and clouds: 2. Model application. *J. Geophys. Res.* 115, B09202. <https://doi.org/10.1029/2009JB007176>.
- Folch, A., Costa, A., Basart, S., 2012. Validation of the FALL3D ash dispersion model using observations of the 2010 Eyjafjallajökull volcanic ash clouds. *Atmos. Environ.* 48: 165–183. <https://doi.org/10.1016/j.atmosenv.2011.06.072>.
- Folch, A., Costa, A., Macedonio, G., 2016. FPLUME-1.0: an integral volcanic plume model accounting for ash aggregation. *Geosci. Model Dev.* 9:431–450. <https://doi.org/10.5194/gmd-9-431-2016>.
- Ganser, G.H., 1993. A rational approach to drag prediction of spherical and non-spherical particles. *Powder Technol.* 77:143–152. [https://doi.org/10.1016/0032-5910\(93\)80051-B](https://doi.org/10.1016/0032-5910(93)80051-B).
- Heath, E., Macdonald, R., Belkin, H., Hawkesworth, C., Sigurdsson, H., 1998. Magmagenesis at Soufriere Volcano, St. Vincent, Lesser Antilles Arc. *J. Petrol.* 39 (10), 1721–1764.
- Jarvis, A., Reuter, H.I., Nelson, A., Guevara, E., 2008. Hole-filled Seamless SRTM Data V4. International Centre for Tropical Agriculture available from. <http://srtm.csi.cgiar.org>.
- Manzella, I., Bonadonna, C., Phillips, J.C., Monnard, H., 2015. The role of gravitational instabilities in deposition of volcanic ash. *Geology* 43 (3):211–214. <https://doi.org/10.1130/G36252.1>.
- Marti, A., Folch, A., Costa, A., Engwell, S., 2016. Reconstructing the Plinian and co-ignimbrite sources of large volcanic eruptions: a novel approach for the Campanian Ignimbrite. *Sci Rep* 6:21220. <https://doi.org/10.1038/srep21220>.
- Mastin, L.G., Van Eaton, A.R., Durant, A.J., 2016. Adjusting particle-size distributions to account for aggregation in tephra-deposit model forecasts. *Atmos. Chem. Phys.* 16: 9399–9420. <https://doi.org/10.5194/acp-16-9399-2016>.
- Morton, B.R., Taylor, G.I., Turner, J.S., 1956. Turbulent gravitational convection from maintained and instantaneous source. *Philos. Trans. R. Soc. Lond. A* 234, 1–23.
- Muerdter, D.R., Dauphin, J.P., Steele, G., 1981. An interactive computerised system for grain size analysis of silt using electro-resistance. *J. Sediment. Petrol.* 51, 647–650.
- Pielke, R.A., Cotton, W.R., Walko, R.L., Tremback, C.J., Nicholls, M.E., Moran, M.D., Wesley, D.A., Lee, T.J., Copeland, J.H., 1992. A comprehensive meteorological modeling system-RAMS. *Meteorol. Atmos. Phys.* 49, 69–91.
- Rose, W.I., Durant, A.J., 2009. Fine ash content of explosive eruptions. *J. Volcanol. Geotherm. Res.* <https://doi.org/10.1016/j.jvolgeores.2009.01.010>.
- Scollo, S., Folch, A., Costa, A., 2008. A parametric and comparative study of different tephra fallout models. *J. Volcanol. Geotherm. Res.* 176:199–211. <https://doi.org/10.1016/j.jvolgeores.2008.04.002>.
- Shepherd, J.B., Sigurdsson, H., 1982. Mechanism of the 1979 explosive eruption of Soufriere volcano, St. Vincent. *J. Volcanol. Geotherm. Res.* 13 (1–2):119–130. [https://doi.org/10.1016/0377-0273\(82\)90023-3](https://doi.org/10.1016/0377-0273(82)90023-3).
- Skamarock, W.C., Klemp, J.B., Dudhia, J., Gill, D.O., Barker, D.M., Duda, M.G., Huang, X.Y., Wang, W., Powers, J.G., 2008. A Description of the Advanced Research WRF Version 3. NCAR Technical Note, NCAR/TN-475 + STR.
- Smoluchowski, M., 1917. *Veruch einer mathematischen Theorie der Koagulationskinetik kolloider Lösungen*. *Z. Phys. Chem.* 92, 128–168.
- Spanu, A., Vitturi, M. de M., Barsotti, S., 2016. Reconstructing eruptive source parameters from tephra deposit: a numerical study of medium-sized explosive eruptions at Etna volcano. *Bull. Volcanol.* 78:59. <https://doi.org/10.1007/s00445-016-1051-2>.
- Sulpizio, R., Folch, A., Costa, A., Scaini, C., Dellino, P., 2012. Hazard assessment of far-range volcanic ash dispersal from a violent Strombolian eruption at Somma-Vesuvius volcano, Naples, Italy: implications on civil aviation. *Bull. Volcanol.* 74:2205–2218. <https://doi.org/10.1007/s00445-012-0656-3>.
- Suzuki, Y., Koyaguchi, T., 2015. Effects of wind on entrainment efficiency in volcanic plumes. *J. Geophys. Res.* 120:6122–6140. <https://doi.org/10.1002/2015JB012208>.
- Ulke, A.G., 2000. New turbulent parameterization for a dispersion model in atmospheric boundary layer. *Atmos. Environ.* 34, 1029–1042.
- Van Eaton, A.R., Muirhead, J.D., Wilson, C.J.N., Cimarelli, C., 2012. Growth of volcanic ash aggregates in the presence of liquid water and ice: an experimental approach. *Bull. Volcanol.* 74:1963–1984. <https://doi.org/10.1007/s00445-012-0634-9>.
- Walker, G.P.L., 1971. Grain-size characteristics of pyroclastic deposits. *J. Geol.* 79, 696–714.
- Yang, C.S., Kao, S.P., Lee, F.B., Hung, P.S., 2004. Twelve different interpolation methods: a case study of SURFER 8.0. *Proceeding of the XXth ISPRS*.